

1

2 **Parameterization and Evaluation of Nonhydrostatic Effect in the**  
3 **Orographic Gravity Wave Drag in China Meteorological**  
4 **Administration Global Forecast System (CMA-GFS) v4.0 Model**

5

6 Rongrong ZHANG<sup>1,2,3</sup>, Zhenzhen AI<sup>1</sup>, Xin XU<sup>1</sup>, Haile XUE<sup>4,5</sup>, Qiyong CHEN<sup>4,5</sup>

7 <sup>1</sup>State Key Laboratory of Severe Weather Meteorological Science and Technology, Key  
8 laboratory of Mesoscale Severe Weather/Ministry of Education, School of Atmospheric Sciences,  
9 Nanjing University, Nanjing 210023, China

10 <sup>2</sup>Jiangsu Meteorological Observatory, Jiangsu Meteorological Bureau, Nanjing 210000, China

11 <sup>3</sup>Jiangsu Key Laboratory of Severe Storm Disaster Risk/Key Laboratory of Transportation  
12 Meteorology of CMA, Nanjing 210000, China

13 <sup>4</sup>State Key Laboratory of Severe Weather Meteorological Science and Technology, CMA Earth  
14 System Modeling and Prediction Centre, Beijing 100081, China

15 <sup>5</sup>Key Laboratory of Earth System Modeling and Prediction, China Meteorological  
16 Administration, Beijing 100081, China

17

18 Correspondence: Xin Xu (xinxu@nju.edu.cn) and Haile Xue (xuehl@cma.cn)

19

20

**Abstract**

21

22

23

24

25

26

27

28

29

30

31

32

33

34

35

36

37

38

39

40

41

42

43

44

The China Meteorological Administration Global Forecast System (CMA-GFS) v4.0 model was upgraded to a higher resolution of  $0.125^\circ$  in May 2023. To be compatible with its fine resolution, the parameterization scheme of orographic gravity wave drag (OGWD) in CAM-GFS is revised herein by accounting for the nonhydrostatic effect (NHE) on the wave momentum flux of subgrid-scale orographic gravity waves. The performance of the revised OGWD scheme is then evaluated for the 10-day medium-range forecast in December 2023. Results show that the revised OGWD scheme can better capture the large-scale circulation in the Northern Hemisphere (NH), particularly in the high latitudes. The easterly (westerly) wind biases in the NH polar stratosphere (troposphere) are decreased. The underestimation of East Asia subtropical jet is also alleviated. Quantitative evaluation shows that the revised OGWD scheme reduces both the mean bias and root mean square error of 500-hPa geopotential height in the NH after the 6th forecast day, reaching 11.59% and 5.06%, respectively, by day 10. The decrease of easterly biases in the polar stratosphere is owing to the weakening of stratospheric zonal OGWD by the NHE. For the decrease of westerly biases in the NH polar troposphere, it is due to the fact that the enhanced stratospheric winds suppress the upward propagation of Rossby waves into the stratosphere, resulting in greater convergence of Eliassen-Palm flux in the mid-upper troposphere.

**Keywords:** orographic gravity wave drag, parameterization, global NWP medium-range forecast

## 45 **1. Introduction**

46 Orographic gravity wave drag (OGWD) is an important process in atmospheric  
47 dynamics, arising from the interaction of airflow with complex terrain (Kim et al., 2003;  
48 Teixeira, 2014). When airstream flows over mountains, it generates orographic gravity  
49 waves (OGWs) which propagate vertically. As these waves break, they transfer  
50 momentum from the surface to higher levels (Fritts and Alexander, 2003). This  
51 momentum transfer plays a crucial role in driving the atmospheric circulation,  
52 influencing both tropospheric and stratospheric dynamics (Alexander et al., 2010).

53 In numerical weather prediction (NWP) and climate models, the OGWD is  
54 typically a subgrid-scale process which needs to be parameterized. Various OGWD  
55 parameterization schemes have been developed over the past few decades (e.g., Palmer  
56 et al., 1986; McFarlane, 1987; Kim and Arakawa, 1995; Lott and Miller, 1997; Scinocca  
57 and McFarlane, 2000; Kim and Doyle, 2005) based on both linear and nonlinear OGW  
58 dynamics. Their implementation has been shown to help alleviate the systematic biases  
59 in both NWP and climate models, ranging from general circulation to regional climate  
60 and weather (e.g., Kim, 2007; McLandress et al., 2012; Choi and Hong, 2015; Zhong  
61 and Chen, 2015; Chen et al., 2016; Lu et al., 2020; Zhang et al., 2020; Li et al., 2023;  
62 Xu et al., 2023; Wei et al., 2025).

63 While accurate representation of OGWD is essential for weather forecast and  
64 climate simulation/projection, traditional OGWD parameterization schemes rely on the  
65 assumption of hydrostatic balance which can significantly simplify the formulae of  
66 OGW dynamics. This assumption is appropriate for coarse-resolution numerical models  
67 where subgrid-scale OGWs are dominated by hydrostatic GWs as the dominant subgrid

68 “mountains” are large. However, as the model resolution increases, the hydrostatic  
69 assumption becomes less valid because the subgrid-scale orography (SSO) becomes  
70 smaller, so that the unresolved GWs have shorter wavelengths. In this situation, the  
71 nonhydrostatic effects (NHEs) will exert remarkable influences on the subgrid-scale  
72 OGWs. Compared with hydrostatic OGWs, nonhydrostatic OGWs experience stronger  
73 horizontal dispersion of wave energy, which reduces wave amplitude and can suppress  
74 wave breaking and momentum deposition into the mean flow (Smith, 1979; Klemp and  
75 Durran, 1983; Zängl, 2003). These NHEs are thus critical for accurately representing  
76 the dynamical impacts of subgrid-scale OGWs in high-resolution models, e.g., the  
77 *state-of-the-art* global NWP models.

78         Recently, Xu et al. (2021) theoretically derived the analytical expressions for  
79 the surface wave momentum flux (WMF) of nonhydrostatic OGWs generated by  
80 idealized three-dimensional orography. They found that the degree of nonhydrostaticity  
81 can be measured by a nondimensional parameter of Froude number which is equal to  
82 the wind speed over the mountain half width and buoyancy frequency, i.e., the inverse  
83 of the nondimensional half-width  $Na/U$  (e.g., Zängl, 2003). Physically, this parameter  
84 represents the ratio between the period of buoyancy oscillation and the time for airflow  
85 travelling through the mountain. The larger the horizontal Froude number, the more  
86 important the NHE is. Based upon the theoretical study, Xu et al. (2023, 2024) revised  
87 the OGWD parameterization scheme developed by Kim and Doyle (2005, hereafter  
88 KD05) by accounting for the NHE on the surface WMF of upward-propagating OGWs.  
89 Then the new OGWD scheme was implemented in the Model for Prediction Across  
90 Scales (MPAS), which was shown to improve the seasonal simulation of the

91 stratospheric polar night jet and reduce the wet biases over the western Tibetan Plateau  
92 in winter. Li et al. (2024) further evaluated the revised OGWD scheme in the Weather  
93 Research and Forecasting (WRF) model for short-range forecast of Northeast China  
94 cold vortices (NECVs). The underestimation of the NECV intensity (in terms of  
95 minimum 500-hPa geopotential height) is alleviated as the NHE decreases the lower-  
96 tropospheric OGWD.

97         The China Meteorological Administration Global Forecast System (CMA-GFS)  
98 is a rename of the Global/Regional Assimilation and Prediction System (GRAPES)  
99 developed in early 2000s (Shen et al., 2017). Operationally running at the CMA Earth  
100 System Modeling and Prediction Center, the CMA-GFS was upgraded to a new version  
101 of v4.0 in May 2023, with its horizontal resolution increasing from about  $0.25^\circ$  to  $0.125^\circ$   
102 (about 13 km), along with many other improvements in the model dynamics and physics  
103 (Shen et al., 2023). For instance, the convective triggering function and quasi-  
104 equilibrium closure conditions are improved to reduce biases in tropics and enhance  
105 forecast skill of precipitation in East Asia. In CMA-GFS, three components of subgrid  
106 scale orography effects have been implemented, i.e., the blocking-flow drag (BFD), the  
107 OGWD and turbulent orographic form drag (TOFD). The TOFD scheme was  
108 implemented CMA-GFS based on Beljaars et al. (2004) and Xue et al. (2011) and will  
109 not be further discussed as it is not relevant to the NHE effect studied in this study. The  
110 BFD component based on Lott and Millor (1997, hereafter LM97) and OGWD  
111 component from Kim and Arakawa (1995, hereafter KA95) were implemented in CMA-  
112 GFS similar to that in Alpert (2004) and was described in Chen et al. (2016). It is  
113 noticed that in the existing implementation, nonhydrostatic effects are only partly reflected

114 through a Scorer-parameter-based partitioning of the momentum stress when the model  
115 grid point is located downstream of the subgrid orography. However, the launch-level  
116 surface WMF itself still follows the original hydrostatic KA95 formulation. In order to be  
117 compatible with its high resolution, this hydrostatic OGWD parameterization scheme  
118 needs to be upgraded to account for the NHE.

119         Note that the present study extends the evaluation of the nonhydrostatic OGWD  
120 scheme in the MPAS model presented in Xu et al. (2024) by transitioning it into a  
121 practical, operational NWP. Although Xu et al. (2024) demonstrated the beneficial  
122 impact of the revised OGWD scheme for long-term, large-scale circulation simulations,  
123 its performance and value within a state-of-the-art, high-resolution global forecasting  
124 system performing routine medium-range forecasts had not been tested. This work  
125 provides this critical assessment using the CMA-GFS v4.0 model, with a specific focus  
126 on forecast skill improvements for several quantitative metrics. The primary advance  
127 lies in evaluating the revised OGWD scheme in reducing systematic forecast biases on  
128 timescales directly relevant to weather prediction (1-10 days). Therefore, this research  
129 bridges the gap between parameterization development and operational implementation,  
130 demonstrating the tangible benefits of incorporating nonhydrostatic effects to improve  
131 medium-range weather forecasting accuracy.

132         The remainder of the paper is organized as follows. Section 2 firstly introduces  
133 the revision of the OGWD parameterization scheme and then describes the setup of the  
134 numerical experiments. Section 3 gives an overall evaluation for the medium-range  
135 forecast of large-scale atmospheric circulation by the CMA-GFS model. The NHE

136 effects on parameterized OGWD and large-scale circulation are examined in section 4.  
 137 Finally, the paper is summarized in section 5 along with discussions.

138

## 139 **2. OGWD parameterization scheme and numerical experiments**

### 140 a. Revision of the KA95 OGWD parameterization scheme

141 The KA95 OGWD considers various aspects of the SSO including its standard  
 142 deviation ( $\sigma_h$ ), orographic asymmetry ( $OA$ ) and orographic convexity ( $OC$ ). The  
 143 surface WMF of OGWs is given by

$$144 \quad \tau_0 = \rho_0 E \frac{m}{\lambda_{eff}} G \frac{|V_0|^3}{N_0}, \quad (1)$$

145 where

$$146 \quad E = (OA + 2)^{C_E \frac{Fr_0}{Fr_c}}, m = (1 + L_x)^{OA+1}, G = \frac{Fr_0^2}{Fr_0^2 + C_G OC^{-1}}, Fr_0 = \frac{\sigma_h N_L}{|V_L|}. \quad (2)$$

147 The variables  $\rho_0$ ,  $|V_0|$  and  $N_0$  are the low-level (from the surface to  $2\sigma_h$ ) mean air  
 148 density, horizontal wind speed and buoyancy frequency. The parameter  $m$  denotes the  
 149 “number of mountains” within the grid cell, characterizing the total volume of SSO  
 150 associated with the orography length ( $L_x$ ). The coefficient  $\lambda_{eff}$  acts as a tunable  
 151 parameter denoting the effective grid length. The transition function  $G$  is an  
 152 enhancement factor for sharp mountains as  $OC$  is large. This scheme also considers the  
 153 effects of low-level wave breaking and/or lee wave trapping through the factor  $E$ , which  
 154 is a function of the shape and location of the SSO within the model grid cell (i.e.,  $OA$ ),  
 155 and the flow nonlinearity (i.e.,  $Fr_0 = \frac{Nh_0}{U}$ ). The two empirical constants are set to  $C_E =$   
 156 0.8 and  $C_G = 0.5$ , which are obtained empirically through a series of numerical  
 157 simulations conducted in Kim and Arakawa (1995).

158 The surface WMF is transported upward level by level until reaching the model  
 159 top or critical level. At each model level, airflow instability is checked according to the  
 160 hypothesis of wave saturation (Lindzen, 1981) and wave-breaking (Miller and Palmer,  
 161 1986).

162 Once the subgrid-scale OGWs saturate and break, they will exert a body force  
 163 on the mean flow through the deposition of wave momentum, namely,

$$164 \quad \frac{d\mathbf{V}(z)}{dt} = \frac{1}{\rho(z)} \frac{\partial \boldsymbol{\tau}(z)}{\partial z}. \quad (3)$$

165 where  $\mathbf{V}(z)$  and  $\boldsymbol{\tau}(z)$  are the mean flow velocity and the WMF at height  $z$ , respectively.  
 166 Note that both the directions of  $\mathbf{V}(z)$  and  $\boldsymbol{\tau}(z)$  are parallel to the mean flow at the low  
 167 level (i.e.,  $\mathbf{V}_L$ ). Readers are referred to KA95 for more details about the scheme.

168 The hydrostatic KA95 scheme above is revised by taking into account the NHE  
 169 on the surface WMF of OGWs, i.e.,

$$170 \quad \tilde{\tau} = \tau_0 [1 + NHE(Fr)]. \quad (4)$$

171  $\tilde{\tau}$  represents the nonhydrostatic surface WMF, where the NHE correction depends only  
 172 on the horizontal Froude number  $Fr = \frac{|\mathbf{v}_0|}{N_0 L_x}$

$$173 \quad NHE(Fr) = -\frac{9}{8} Fr^2 + e^{-2Fr^{-1}} \left( -\frac{5}{4} Fr^{-2} - \frac{1}{2} Fr^{-1} + \frac{5}{4} + \frac{9}{4} Fr + \frac{9}{8} Fr^2 \right). \quad (5)$$

174 Eq. (5) is adopted from Xu et al. (2021) for three-dimensional isotropic terrain. Specifically,  
 175 the nonhydrostatic correction is defined as the ratio of the analytically derived  
 176 nonhydrostatic surface WMF to its hydrostatic counterpart, which yields an algebraic  
 177 correction factor depending only on the horizontal Froude number. Note that the  
 178 horizontal Froude number is different from the traditional Froude number  $Fr_0$  above  
 179 which measures the flow nonlinearity. While Xu et al. (2021) have derived the fully

180 NHE for anisotropic terrain, the expressions involve complicated integrals that are not  
181 suitable for practical use in parameterization [cf. their Eqs. (14) to (17)]. Xu et al. (2021)  
182 demonstrated that terrain anisotropy only has a very weak influence on the NHE, so the  
183 expression of NHE for isotropic terrain, i.e., Eq. (5), is used because of simplicity, since  
184 only algebraic manipulations are involved. This is in agreement with Xu et al. (2023,  
185 2024) and Li et al. (2024).

186

#### 187 b. Setup of numerical experiments

188 The CMA-GFSv4.0 dynamical core is based upon the nonhydrostatic and  
189 shallow atmospheric governing equations in spherical polar coordinates with full  
190 physics packages (Shen et al., 2020). It adopts a regular latitude-longitude grid of  
191  $0.125^\circ \times 0.125^\circ$  with *C*-grid staggering. In the vertical, a terrain-following height-based  
192 grid is utilized along with Charney-Phillips staggering. There are 87 vertical levels,  
193 with the model top located at 73 km. For model physics, the Liu-Ma microphysics  
194 scheme (Ma et al., 2018) is employed, along with the RRTMG longwave and shortwave  
195 radiation schemes (Morcrette et al., 2008), the MRF planetary boundary layer scheme  
196 (Chen et al. 2020; Hong and Pan 1996), the CoLM land surface model (Dai et al., 2003),  
197 NSAS convection scheme (Han and Pan, 2011; Liu et al., 2015), the combined KA95  
198 OGWD and LM97 FBD parameterization scheme (Chen et al., 2016), and modified  
199 Beljaars's TOFD scheme (Xue et al., 2011).

200 In order to examine the impact of the revised OGWD scheme on the medium-  
201 range forecast, two sets of numerical simulations (i.e., EXP\_CTL and EXP\_NHE) are  
202 conducted with different OGWD parameterization schemes, using the original KA95

203 scheme and the revised nonhydrostatic one, respectively. Both experiments consist of 31  
204 individual forecasts, each initialized at 00 UTC for the days from 1 to 31 December 2023.  
205 Herein, a winter month is chosen because the OGWD, which is mainly located in the  
206 Northern Hemisphere (NH) given the pronounced orography, is the strongest in this  
207 season (e.g., Xu et al. 2020; Lu et al. 2024). In each experiment, the CMA-GFS model  
208 is integrated for 10 days, i.e., medium-range forecast, with 6-hr output interval. The  
209 model initial conditions are derived from the  $0.25^\circ \times 0.25^\circ$  ECMWF Reanalysis v5 (ERA5)  
210 dataset (Hersbach et al., 2020), which are also used as reference for the evaluation of the  
211 CMA-GFS forecasts. Although the horizontal resolution of ERA5 is coarser than that of  
212 the CMA-GFS v4.0 simulations, ERA5 is adopted here as the verification reference  
213 because it is a dynamically consistent reanalysis constrained by a broad range of  
214 assimilated observations. In this study, ERA5 is not used to resolve the non-hydrostatic  
215 subgrid-scale orographic gravity waves themselves. Instead, it serves as a benchmark for  
216 evaluating the large-scale circulation response and medium-range forecast skill associated  
217 with the revised OGWD parameterization.

218

### 219 **3. Evaluation of the medium-range forecast**

#### 220 *a. Atmospheric circulation*

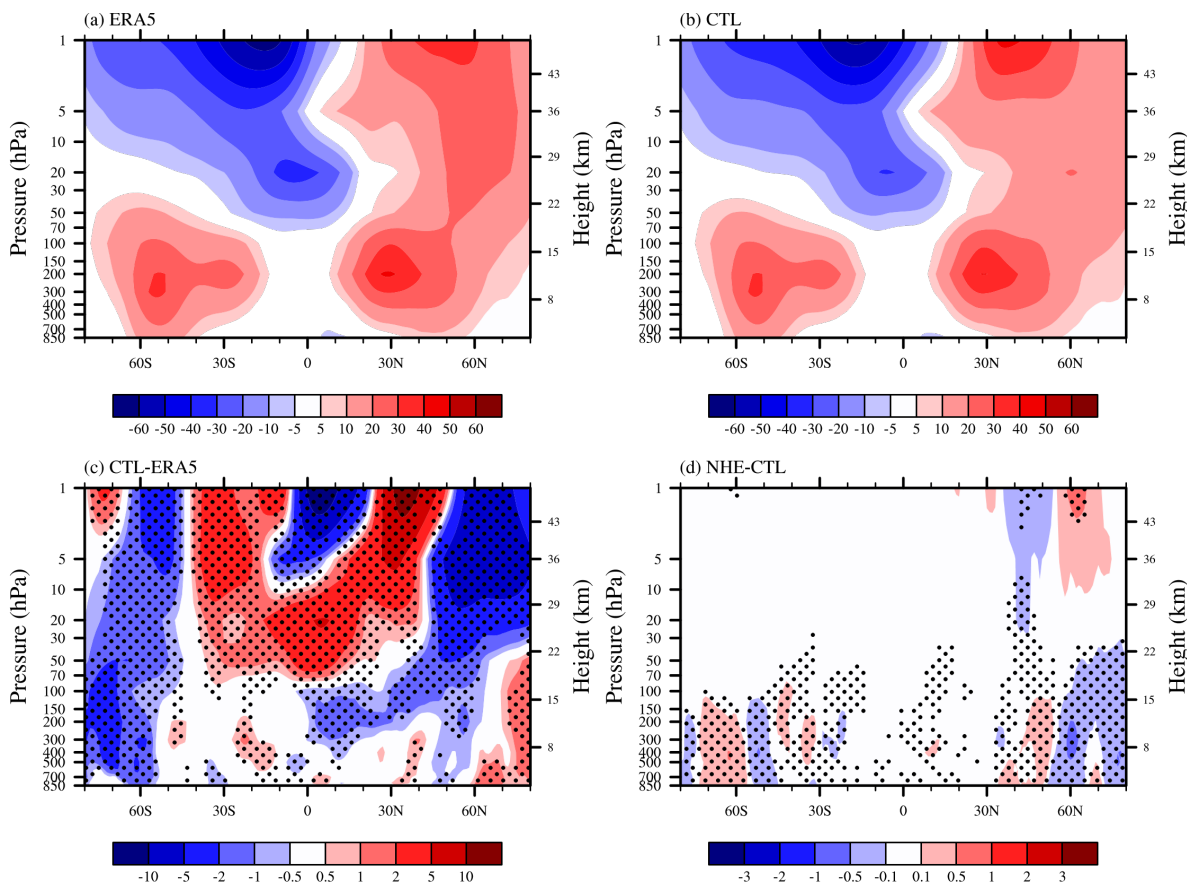
221 Figure 1 shows the zonal-mean zonal wind composited from the day 10 forecast  
222 output of the 31 simulations initialized at 00 UTC on 1-31 December 2023. Accordingly,  
223 the valid times of these day-10 forecasts span 10 December 2023 to 10 January 2024 (i.e.,  
224 the 10th day of the medium-range forecast). In the winter of NH, as revealed by the  
225 ERA5 reanalysis (Fig. 1a), there is a subtropical jet in the midlatitudes troposphere and

226 stratosphere, with the jet core located at about 200 hPa and 30°N. The maximum zonal  
227 wind speed exceeds 35 m s<sup>-1</sup>. In the stratosphere of high latitudes, there is another wind  
228 maxima near 1 hPa and 60°N, which is the well-known polar-night jet (e.g., Kim, 2007)..  
229 In the Southern Hemisphere (SH), which is in summer, there is also a upper tropospheric  
230 lower stratospheric jet but relatively weaker and lower than in the NH. The SH jet core  
231 is located at about 50°S, with a secondary one near 30°S. During austral summer, the  
232 SH stratosphere is dominated by easterlies, which is distinctly different from the NH. With  
233 a center located near 1 hPa and 20°S, the stratospheric easterlies extend downward and  
234 equatorward to the tropics. An easterly jet of over -30 m s<sup>-1</sup> can be found near 20 hPa  
235 and 5°S.

236 Figure 1b is similar to Figure 1a but for the zonal-mean zonal winds obtained in  
237 the EXP\_CTL experiment. In general, the CMA-GFS model can capture the overall  
238 pattern of the zonal-mean zonal winds, such as the tropospheric westerly jets in both  
239 hemispheres and the easterly winds in the SH stratosphere. The polar night jet in the  
240 NH, however, is underestimated by the model, with the jet core shifted southward by  
241 about 10 latitudes. As shown in Fig. 1c, there are notable easterly biases of over -5 m  
242 s<sup>-1</sup> in the stratosphere of the NH high latitudes (north of 50°N). By contrast, westerly  
243 biases are present in the upper stratosphere of the NH midlatitudes (25°N-50°N) which  
244 can exceed 10 m s<sup>-1</sup>, extending downward and equatorward to the lower stratosphere of  
245 the tropics. Similarly, the zonal-mean zonal winds in the NH troposphere are  
246 overestimated in the Arctic region, but with easterly biases in the mid-lower latitudes.  
247 In the SH, the stratospheric easterlies are shifted northward, leading to westerly biases  
248 in the mid-lower latitudes (40°S-5°S) and easterly biases in the tropics and lower

249 latitudes of the NH ( $5^{\circ}\text{S}$ - $20^{\circ}\text{N}$ ). In the high latitudes, there are predominantly easterly  
250 biases in both troposphere and stratosphere except in the upper stratosphere over the  
251 polar cap.

252         When taking into account the NHE in the OGWD parameterization scheme, the  
253 CMA-GFS model can better capture the large-scale circulation. Figure 1d presents the  
254 differences between the zonal-mean zonal winds in the two numerical experiments (i.e.,  
255 EXP\_NHE minus EXP\_CTL). In the stratosphere above  $\sim 10$  hPa, positive and negative  
256 wind differences are found to the north and south of  $60^{\circ}\text{N}$ , respectively, which are just  
257 opposed to the wind biases in Figure 1c. It suggests that both the magnitude and location  
258 of the polar night jet are improved. For example, the NH easterly biases in the mid-  
259 upper stratosphere ( $\sim 10$  hPa to 1 hPa) are reduced by about 3%. The westerly biases in  
260 the troposphere of Arctica region are also reduced, which reaches up to about 42% of  
261 the total bias. At the same time, the easterly wind biases in the mid-latitude troposphere  
262 have also reduced.



263

264 Figure 1. Vertical distributions of zonal-mean zonal wind (units:  $\text{m s}^{-1}$ ) averaged in the  
 265 period of 10 December 2023 to 10 January 2024 obtained from (a) ERA5 and (b)  
 266 EXP\_CTL, with their difference (i.e., EXP\_CTL minus ERA5) given in (c). (d) is  
 267 similar to (c) but for the difference between the two experiments of EXP\_NHE and  
 268 EXP\_CTL (i.e., EXP\_NHE minus EXP\_CTL). Stippling in (c) and (d) denote  
 269 differences statistically significant at the 95% confidence level.

270

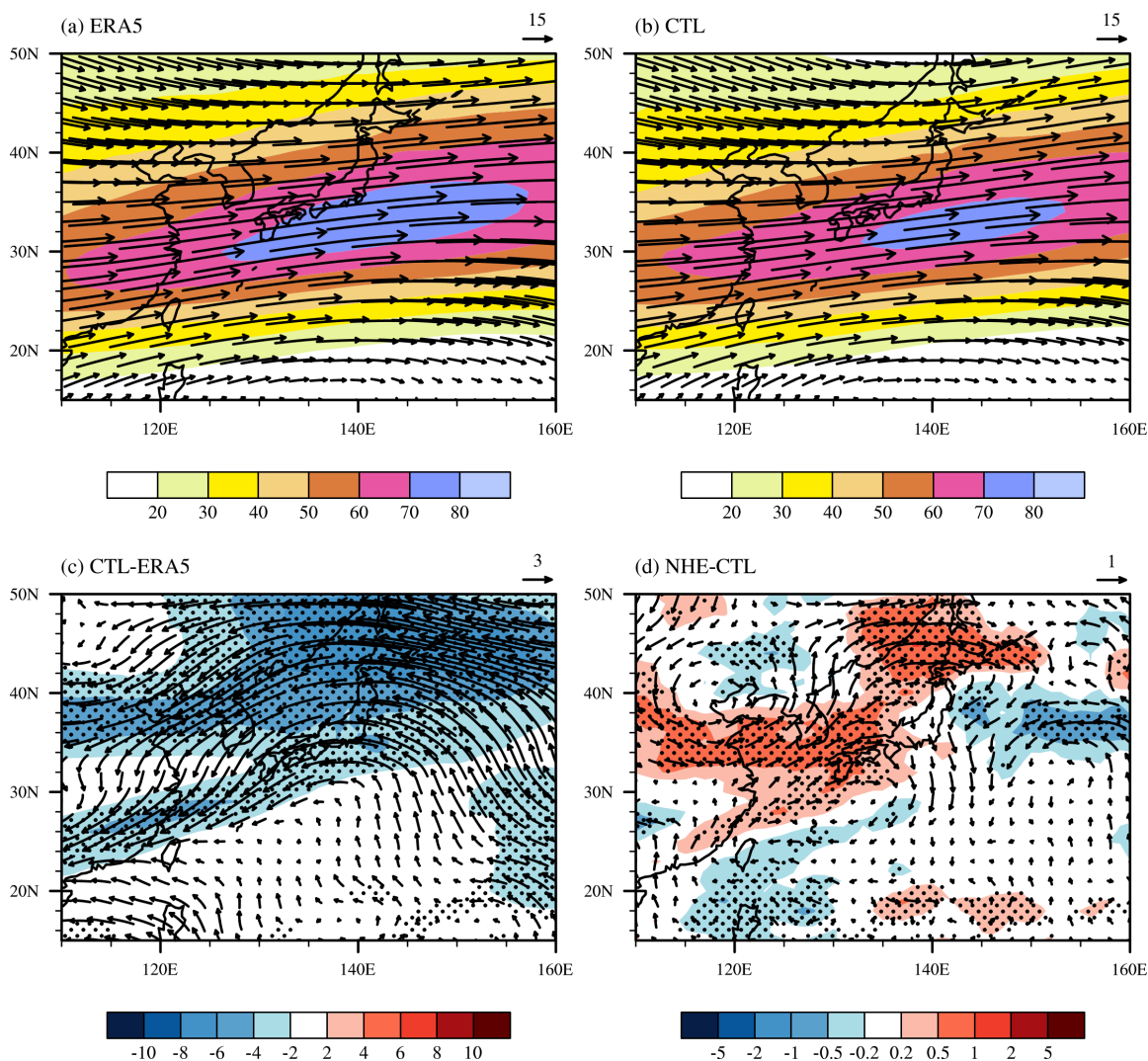
271 For the zonal-mean zonal wind biases in the SH stratosphere, they are hardly  
 272 alleviated, however. This is because the stratospheric OGWD is very weak in summer  
 273 (see Fig. 5a of Xu et al. 2024; see also Fig. 3 below), given the absorption of OGWs at  
 274 the critical level (Booker and Bretherton, 1967), that is, the zero-wind level between  
 275 the tropospheric westerlies and the stratospheric easterlies (Fig. 1a). The easterly biases  
 276 in the troposphere of the high latitudes are reduced, especially around  $60^{\circ}\text{S}$ .

277           Although there is no significant improvement for the zonal-mean zonal wind in  
278 the NH mid-lower latitudes (Fig. 1d), the wind circulation can be improved regionally,  
279 such as the East Asia subtropical jet (EASJ). Figure 2a shows the horizontal wind field  
280 and speed at 200 hPa averaged in the period of 10 December 2023 to 10 January 2024  
281 from the ERA5 reanalysis. In boreal winter, the EASJ stretches from about 110°E to  
282 160°E in the latitudes between about 25°N and 45°N. The jet core is located near Japan,  
283 showing a high wind speed of over 70 m s<sup>-1</sup>. The simulated EASJ in the EXP\_CTL  
284 experiment generally aligns well with the ERA5 reanalysis, in terms of its location and  
285 orientation (Fig. 2b). But the jet intensity is underestimated, showing easterly biases of  
286 over -4 m s<sup>-1</sup> (Fig. 2c). In the EXP\_NHE experiment, the underestimation of the EASJ  
287 is alleviated, with the mean bias decreased by about 6% (Fig. 2d).

288

289

290



291

292 Figure 2. Horizontal distributions of wind speed (shading; units:  $\text{m s}^{-1}$ ) and wind field  
 293 (arrow) at 200 hPa averaged in the period of 10 December 2023 to 10 January 2024  
 294 obtained from (a) ERA5 and (b) EXP\_CTL, with their difference (i.e., EXP\_CTL minus  
 295 ERA5) given in (c). (d) is similar to (c) but for the difference between the two  
 296 experiments of EXP\_NHE and EXP\_CTL (i.e., EXP\_NHE minus EXP\_CTL).  
 297 Stippling in (c) and (d) denote differences statistically significant at the 95% confidence  
 298 level.

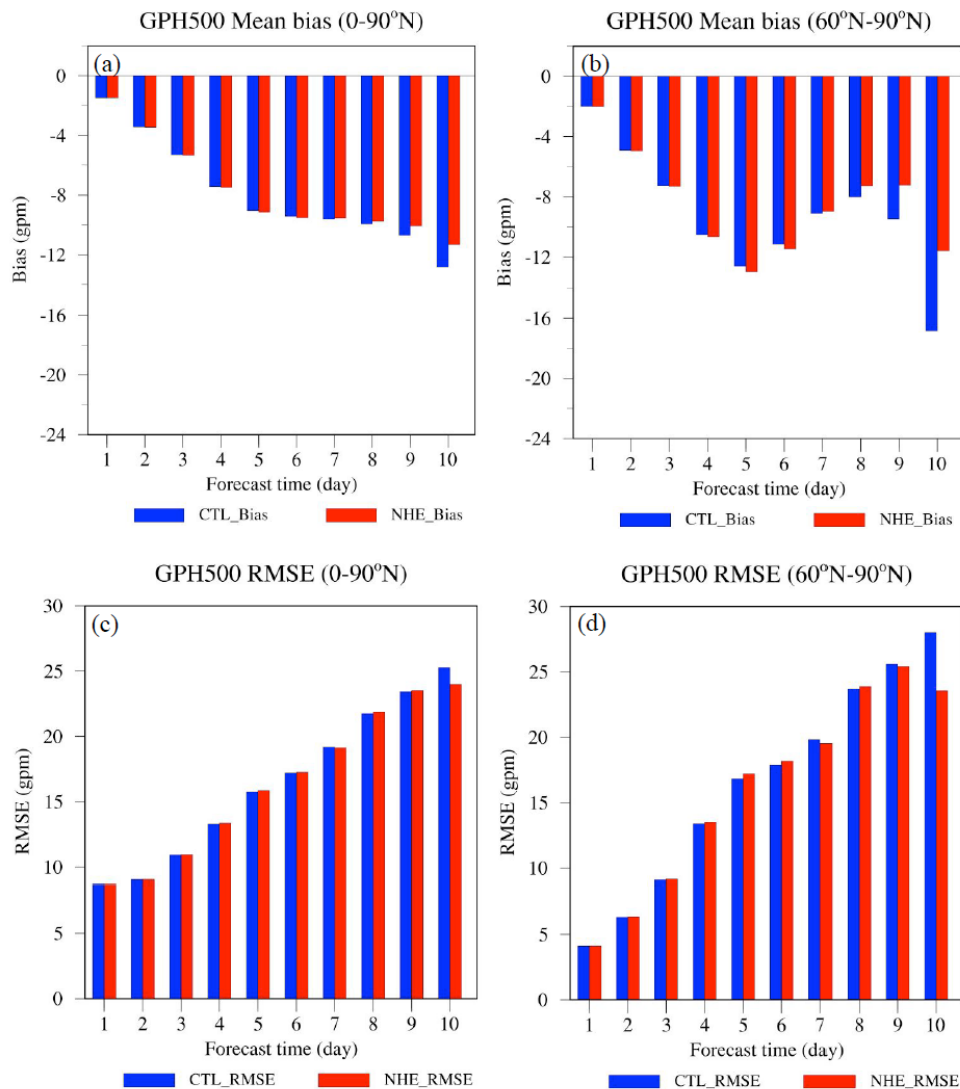
299

300

301

302 *b. Quantitative evaluation of forecast skills*

303 For medium-range forecast, the wind circulation in the troposphere is often of  
 304 greater interest than in the stratosphere. To better evaluate the performance of the  
 305 revised OGWD scheme, Figures 3a and 3b depict the mean bias (MB) and root mean  
 306 square error (RMSE) for the 500 hPa geopotential height (GPH500) in the two  
 307 experiments. Herein, we are interested in the NH because of the relatively weak wind  
 308 differences in the SH (Fig. 1d) which is mainly covered by the ocean. Moreover, as will  
 309 be shown below, the parameterized OGWD changes little in the SH.

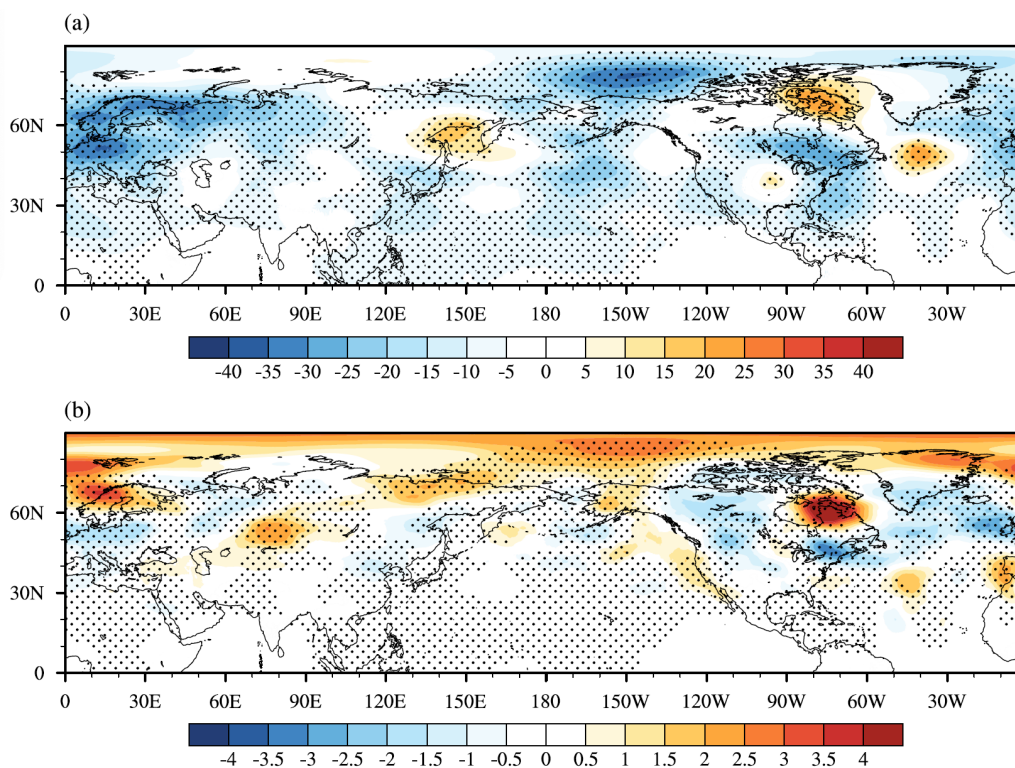


310

311 Figure 3. (a) Mean bias and (c) RMSE of the GPH500 in the NH at different forecast  
312 lead time. (b) and (d) are similar to (a) and (c) but in the region north of 60°N.

313

314 In both experiments, the model GPH500 is lower than the ERA5 reanalysis, with  
315 the MB and RMSE increasing with the forecast lead time (Figs. 3a, 3c). The GPH500  
316 shows obvious underestimation in the EXP\_CTL experiment which are significantly  
317 reduced in EXP\_NHE. This improvement is particularly evident in high latitudes north  
318 of 60°N which is overall statistically significant at the 95% confidence level (Figs. 4a,  
319 4b). Compared to EXP\_CTL, EXP\_NHE exhibits even greater MB and RMSE of  
320 GPH500 till the 6th forecast day. Nevertheless, both the MB and RMSE of the GPH500  
321 decrease quickly afterwards, which are reduced by 11.59% and 5.06%, respectively, at  
322 the 10th day of the forecast (Table 1). Greater improvements are found for the GPH500  
323 between 60°N and 90°N, the MB and RMSE of which are decreased by 31.18% and  
324 15.93%, respectively, at the 10th forecast day (Table 1). All the values shown in Table  
325 1 are statistically significant at the 95% confidence level. For the total 10 forecast days  
326 as a whole, the MB and RMSE of GPH500 are separately reduced by 2.6% and 0.52 %,  
327 indicating an overall improvement in the simulation of the large-scale circulation in the  
328 NH when using the revised OGWD scheme (see Table 2).



329

330 Figure 4. (a) Mean biases of GPH500 (shading; units: gpm) in EXP\_CTL experiment  
 331 as compared to ERA5 averaged over the ten forecast days. (b) is similar to (a) but for  
 332 the differences between the GPH500 (shading; units: gpm) in EXP\_CTL and  
 333 EXP\_NHE experiments (i.e., EXP\_NHE minus EXP\_CTL). Stippling in (a) and (b)  
 334 denote differences statistically significant at the 95% confidence level.

335

336 Table 1. Mean bias and RMSE of the 500-hPa geopotential height (GPH500) and sea  
 337 level pressure (SLP) at the 10th forecast day

	Region	Mean Bias			RMSE		
		CTL	NHE	$\frac{NHE - CTL}{CTL} \times 100$	CTL	NHE	$\frac{NHE - CTL}{CTL} \times 100$
GPH500 (gpm)	0-90°N	-12.825	-11.338	-11.59	25.263	23.984	-5.06
	60°N-90°N	-16.841	-11.590	-31.18	28.017	23.554	-15.93
SLP (hPa)	0-90°N	-0.522	-0.343	-34.29	2.714	2.515	-8.33
	60°N-90°N	-1.712	-1.079	-36.97	3.049	2.517	-17.45

338

339 Table 2. Mean bias and RMSE of the 500-hPa geopotential height (GPH500) and sea  
 340 level pressure (SLP) for the overall ten forecast days

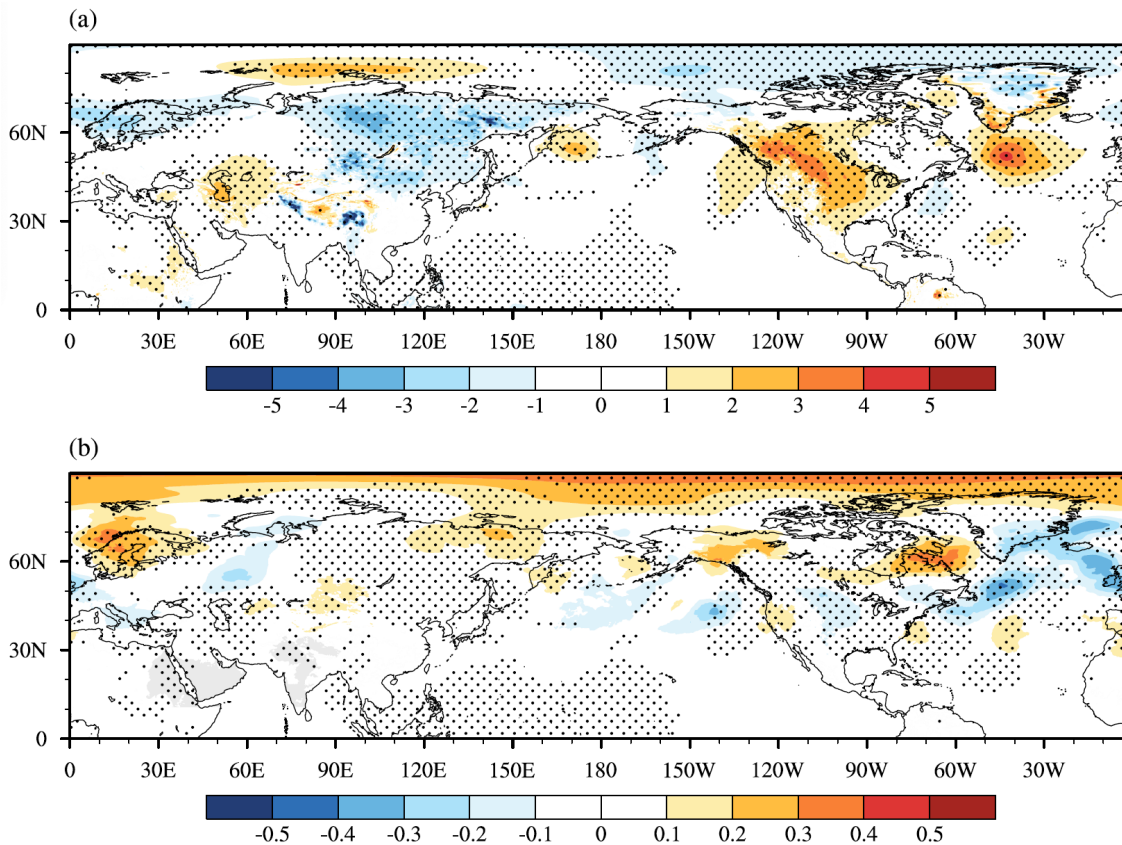
		Mean Bias			RMSE		
	Region	CTL	NHE	$\frac{NHE - CTL}{CTL} \times 100$	CTL	NHE	$\frac{NHE - CTL}{CTL} \times 100$
GPH500 (gpm)	0-90°N	-7.923	-7.717	-2.6	16.455	16.369	-0.52
	60°N-90°N	-9.187	-8.438	-8.15	16.470	16.089	-2.31
SLP (hPa)	0-90°N	-0.107	-0.082	-23.46	1.87	1.841	-1.53
	60°N-90°N	-0.498	-0.411	-17.47	1.598	1.532	-4.13

341

342 Besides the GPH500, the forecast skill is also examined for the SLP in the NH.  
 343 As shown in Fig. 5a, the EXP\_CTL experiment systematically underestimates the SLP  
 344 over East Asia and the Arctic, while overestimating SLP across North America and the  
 345 northern Atlantic. These biases are substantially corrected in the EXP\_NHE experiment,  
 346 particularly in high-latitude regions north of 60°N (Fig. 5b). Similarly, the EXP\_NHE  
 347 experiment firstly experiences a degradation in the early 6 days compared to EXP\_CTL,  
 348 but it shows significant improvement at the end of the 10th forecast day, with the MB  
 349 reduced by 34.29% and the RMSE by 8.33%, respectively (Table 1). Greater decreases  
 350 of 36.97% (for MB) and 17.45% (for RMSE) are found in the high latitudes north of  
 351 60°N as well.

352

353



354

355 Figure 5. (a) Mean biases of SLP (shading; units: hPa) in the EXP\_CTL experiment as  
 356 compared to ERA5 averaged over the ten forecast days. (b) is similar to (a) but for the  
 357 differences between the SLP (shading; units: hPa) in the EXP\_CTL and EXP\_NHE  
 358 experiments (i.e., EXP\_NHE minus EXP\_CTL). Stippling in (a) and (b) denote  
 359 differences statistically significant at the 95% confidence level.

360

361 From the above analyses, implementing the revised OGWD scheme in the high-  
 362 resolution CMA-GFS model can help improve the medium range forecast of the NH  
 363 large-scale circulation, especially in the high latitudes. In the next section, we will  
 364 examine the underlying mechanisms responsible for the improvement of the circulation.

365

366

## 367 **4. Physical interpretation**

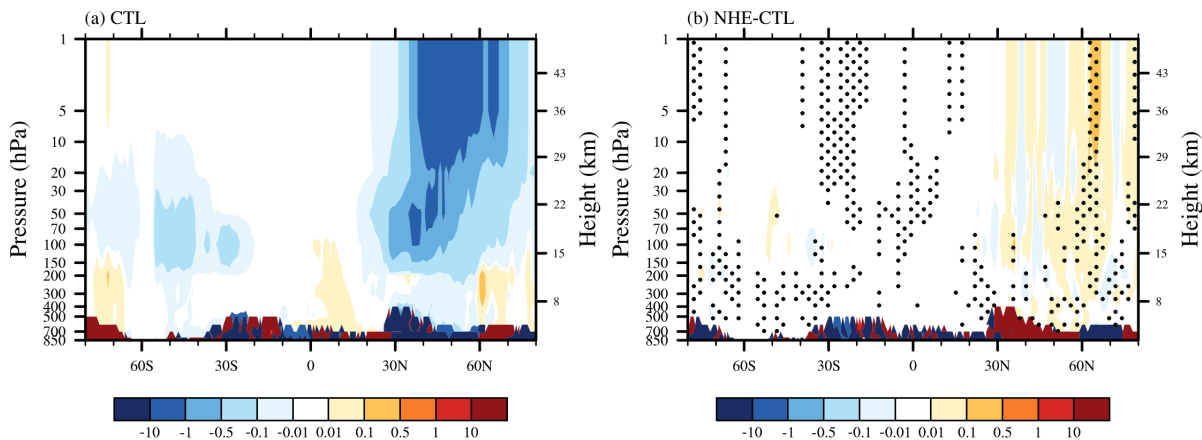
### 368 *a. Changes of parameterized OGWD*

369           The changes of wind circulation arise from the revision of the OGWD scheme.  
370 It is thus straightforward to study the parameterized OGWD in these two experiments.  
371 Figure 6a shows the vertical distribution of zonal-mean zonal OGWD averaged in the  
372 period of 10 December 2023 to 10 January 2024 in the EXP\_CTL experiment. The  
373 differences between the parameterized OGWD in the two experiments (i.e., EXP\_NHE  
374 minus EXP\_CTL) are given in Fig. 6b. In boreal winter, there exists prominent OGWD  
375 in the stratosphere of the NH mid-to-high latitudes, which is favored by the decrease of  
376 air density with height (e.g., Lindzen, 1981) and the relatively weak winds between the  
377 tropospheric jet and polar night jet. The latter is called as the “valve layer” by Kruse et  
378 al. (2016). The maximum OGWD occurs between about 20 hPa and 1 hPa. In contrast,  
379 there is very weak OGWD in the SH stratosphere owing to the critical level absorption  
380 as mentioned above.

381           Compared to that in EXP\_CTL, the zonal-mean zonal OGWD in EXP\_NHE is  
382 generally weakened in the high latitudes of the NH (north of about 55°N), especially in  
383 the stratosphere (Fig. 6b). Note that the positive difference indicates a decrease of  
384 OGWD as the drag itself is negative. This is due to the fact that the NHE acts to decrease  
385 the surface WMF [see Eqs. (4) and (5)], i.e., the source of parameterized OGWs which  
386 determines the maximum wave momentum that can be deposited into the mean flow.  
387 Therefore, the decrease of surface WMF is prone to reduce the OGWD. Note that there  
388 is also enhancement of OGWD, e.g., in the stratosphere near 50°N. This may be  
389 attributed to a decrease in surface WMF, which suppresses tropospheric wave breaking

390 by lowering the gravity-wave amplitude limit for breaking at lower levels and thus  
 391 shifts the wave-breaking altitude upward. Consequently, a vertical structure  
 392 characterized by alternating positive-negative-positive anomalies from the surface to  
 393 the stratosphere would be expected. In consequence, more WMF is transported to the  
 394 stratosphere where the OGWs break owing to the decay of air density and lead to  
 395 stronger OGWD. This is similar to the redistribution of WMF in the vertical owing to  
 396 selective critical level filtering of OGWs in directional shear flows (Shutts, 1995; Xu  
 397 et al., 2012, 2019; van Niekerk et al., 2023). Generally, the changes in the vertical  
 398 structure of parameterized OGWD in the CMA-GFS model are similar to that in the  
 399 MPAS seasonal simulations conducted in Xu et al. (2024) which also considers the  
 400 NHE correction to the OGWD (cf. their Fig. 5). **Instead, the lower-tropospheric OGWD**  
 401 **is also affected by the interaction and feedback between model dynamics and physical**  
 402 **parameterizations. Changes in the simulated low-level circulation, including possible**  
 403 **meridional displacement of drag-producing flow configurations, can modify the wind**  
 404 **speed, stability, and mountain-flow orientation sampled by the OGWD scheme, thereby**  
 405 **producing localized enhancement of the near-surface drag in EXP\_NHE.**

406



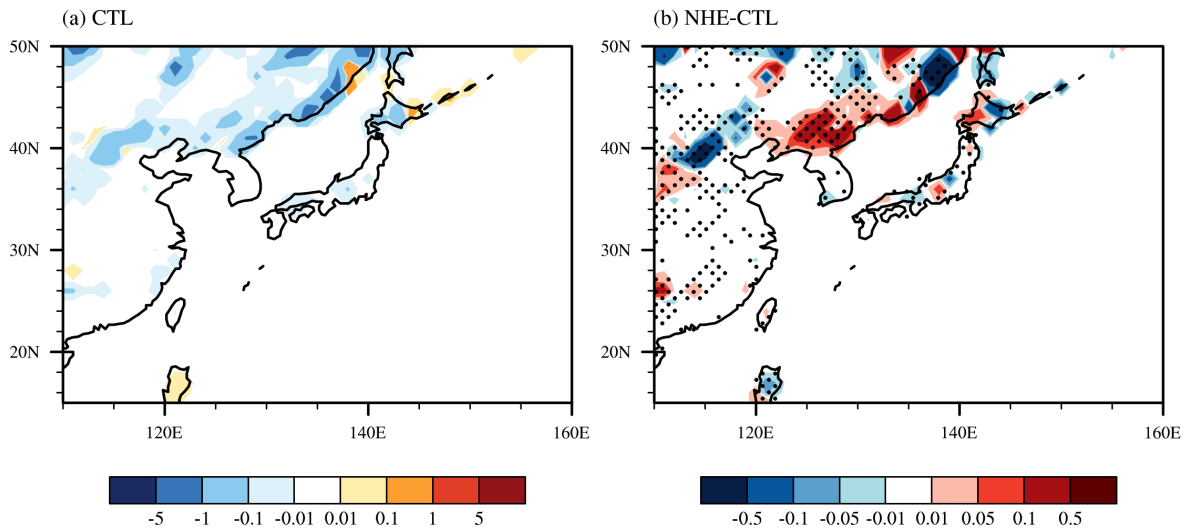
407

408 Figure 6. Vertical distributions of (a) zonal-mean zonal OGWD (units:  $\text{m s}^{-1} \text{ day}^{-1}$ )  
409 averaged in the period of 10 December 2023 to 10 January 2024 obtained from  
410 EXP\_CTL, and (b) zonal-mean OGWD difference between the two experiments of  
411 EXP\_NHE and EXP\_CTL (i.e., EXP\_NHE minus EXP\_CTL). Stippling in (b) denotes  
412 differences statistically significant at the 95% confidence level.

413

414         The weakening of OGWD can directly increase the zonal winds in the polar  
415 stratosphere and the mid-latitude troposphere of the NH, thus leading to a recover of  
416 the weakened westerly jet. Conversely, the enhancement of OGWD can directly weaken  
417 the zonal winds in the mid-latitude stratosphere and the polar troposphere of the NH,  
418 thereby reducing the westerly biases (Figs. 1c, 1d). The parameterized OGWD in East  
419 Asia is also examined to explain the changes of EASJ. As shown in Fig. 7a, there is  
420 notable westward OGWD at 200 hPa in the high latitudes of East Asia where the  
421 underlying terrain is very complex, such as the Taihang, Yanshan, Changbai, Greater  
422 Khingan and Lesser Khingan Mountains. Thus, the largest easterly biases of the EASJ  
423 occur in this region (Fig. 2c). When accounting for the NHE in the OGWD  
424 parameterization scheme, the 200-hPa OGWD is mainly reduced (Fig. 7b). Clearly, the  
425 enhanced EASJ is owing to the weakening of the parameterized OGWD.

426



427

428 Figure 7. Horizontal distributions of (a) zonal OGWD (units:  $\text{m s}^{-1} \text{ day}^{-1}$ ) at 200 hPa  
 429 averaged in the period of 10 December 2023 to 10 January 2024 obtained from  
 430 EXP\_CTL, and (b) zonal OGWD difference between the two experiments of EXP\_NHE  
 431 and EXP\_CTL (i.e., EXP\_NHE minus EXP\_CTL) at 200 hPa. Stippling in (b) denotes  
 432 differences statistically significant at the 95% confidence level.

433

#### 434 *b. Resolved Rossby-wave adjustment*

435 In addition to the direct effect of the modified OGWD, the tropospheric response  
 436 in the Northern Hemisphere is also associated with an adjustment of resolved large-scale  
 437 Rossby waves. This interpretation is consistent with the wave-drag compensation and  
 438 propagation-adjustment mechanisms discussed in previous studies (e.g., Cohen et al., 2013;  
 439 Sigmond and Shepherd, 2014). In particular, changes in the background zonal wind may  
 440 alter the propagation conditions for planetary waves and thereby redistribute the resolved  
 441 wave forcing between the troposphere and stratosphere.

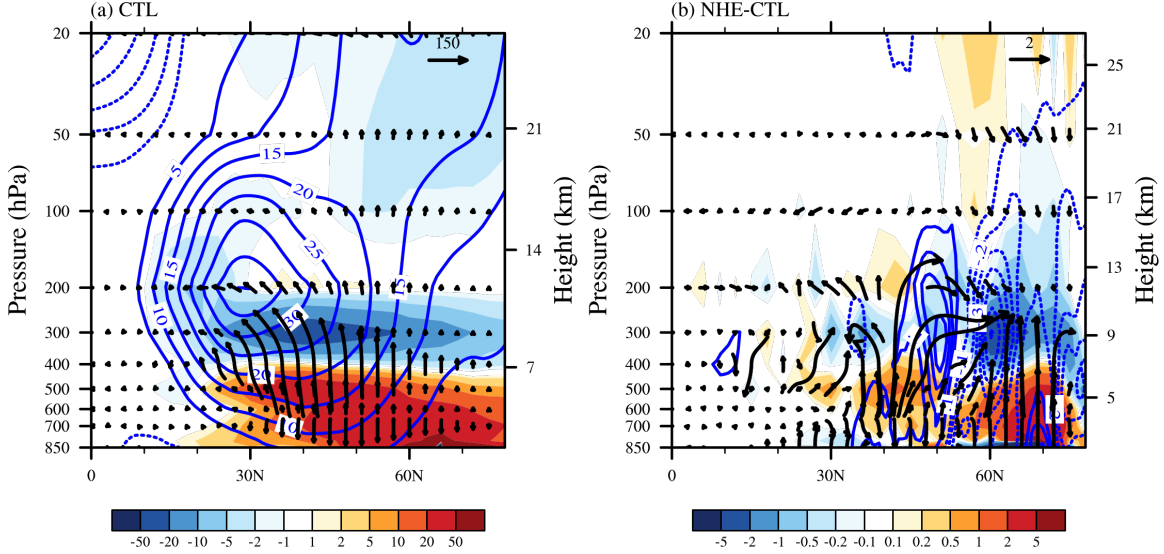
442 It is well known that the impacts of large-scale Rossby waves on the mean flow  
 443 can be measured by the convergence of the zonal-mean Eliassen-Palm (EP) flux. Figure  
 444 8a illustrates the distribution of the zonal-mean EP flux in the EXP\_CTL experiment

445 which is calculated following Edmon et al. (1980). In the NH middle-to-high latitudes,  
446 Rossby waves originate from the lower troposphere which propagate upward and  
447 converge in the upper troposphere. These waves split into two branches in the lower  
448 stratosphere. The first branch turns to propagate equatorward across the tropospheric  
449 jet. The other branch continues to propagate upward to the upper stratosphere where  
450 the EP flux is converged and decelerates the mean flow. As in the SH, the Rossby waves  
451 cannot propagate into the stratosphere (not shown) because of the presence of easterlies  
452 there during austral summer (Fig. 1a).

453 Figure 8b is similar to Fig. 8a but gives the differences between the zonal-mean  
454 EP fluxes in the two experiments (i.e., EXP\_NHE minus EXP\_CTL). Compared to  
455 EXP\_CTL, the upward propagation of Rossby waves into the stratosphere is suppressed  
456 in the high latitudes of the NH, leading to an enhanced convergence of EP flux in the  
457 troposphere. As a result, the zonal-mean zonal winds in the NH polar troposphere are  
458 decelerated by the large-scale Rossby wave forcing, which contributes to the alleviation  
459 of westerly biases there (Figs. 1c, 1d). This may explain why the improvements in the  
460 GPH 500 forecast emerge after 6 days in EXP\_NHE (Fig. 2). The Rossby waves and  
461 their interaction with the mean flow require several days to develop fully and influence  
462 the large-scale circulation.

463

464



465

466 Figure 8. Vertical distributions of zonal-mean EP flux (vectors) and its divergence  
 467 (shading;  $\text{m s}^{-1} \text{ day}^{-1}$ ) due to resolved waves averaged in the period of 10 December  
 468 2023 to 10 January 2024 obtained from (a) EXP\_CTL, and (b) the difference between  
 469 the two experiments of EXP\_NHE and EXP\_CTL (i.e., EXP\_NHE minus EXP\_CTL).  
 470 Contours are the corresponding zonal-mean zonal wind (units:  $\text{m s}^{-1}$ ).

471

472 The suppressed upward propagation of Rossby waves can be understood from  
 473 the changes of the refractive index ( $RFI$ ) that measures the ability of Rossby wave  
 474 propagation (e.g., Chen and Robinson, 1992; Hu et al., 2019), which is defined as

$$475 \quad RFI = \left[ \frac{\overline{q_\phi}}{r\overline{U}} - \left( \frac{k}{r\cos\phi} \right)^2 - \left( \frac{f}{2NH} \right)^2 \right] r^2, \quad (6)$$

476 where  $\overline{U}$ ,  $k$  and  $H$  are the resolved zonal-mean zonal wind, zonal wave number and density  
 477 scale height, respectively.  $\overline{q_\phi}$  represents the meridional gradient of the potential vorticity,  
 478 which is expressed in the following form of

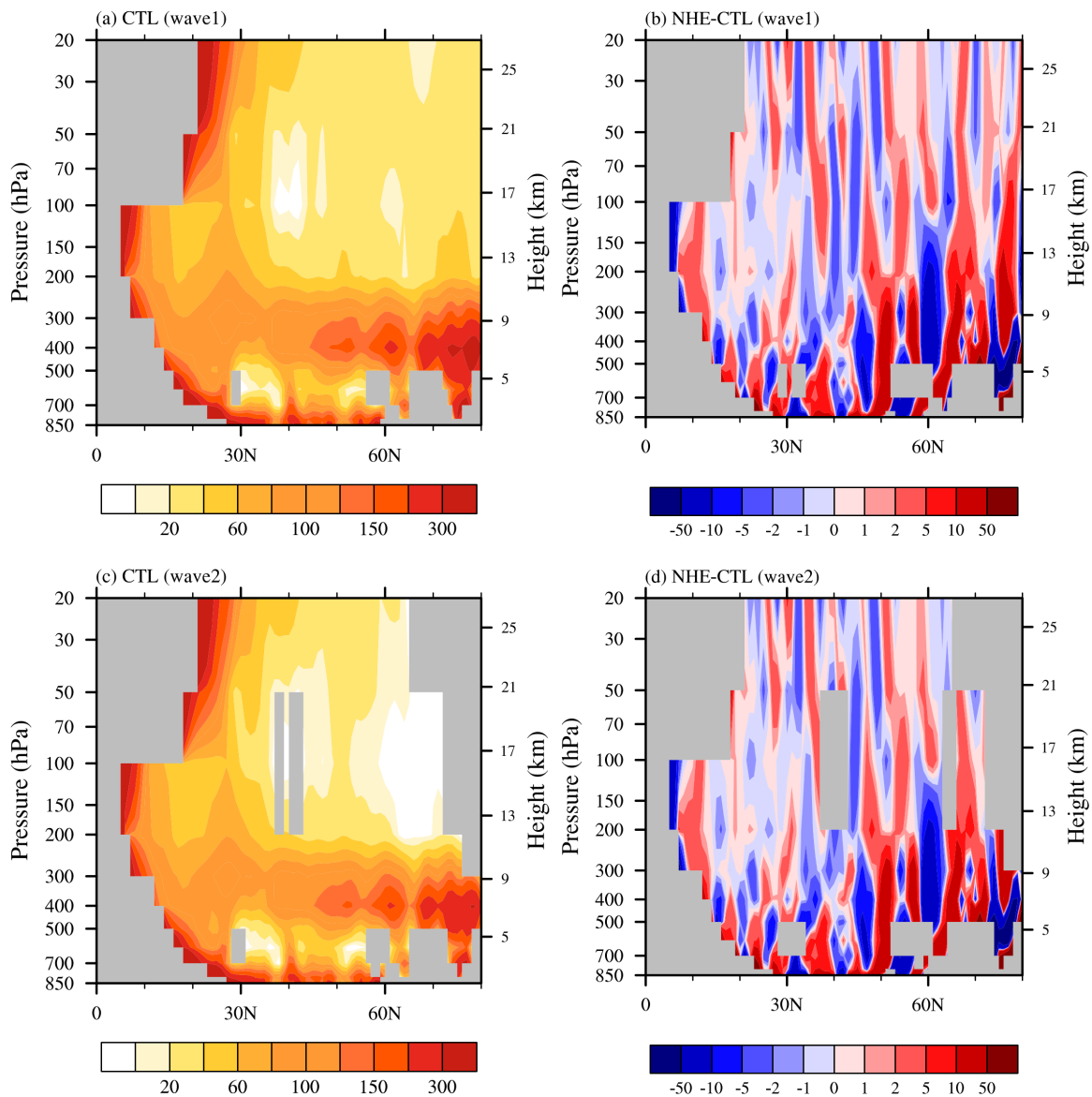
$$479 \quad \overline{q_\phi} = 2\Omega\cos\phi - \left[ \frac{(\overline{U\cos\phi})_\phi}{a\cos\phi} \right]_\phi + \frac{af^2}{Ra} \left( \frac{p\theta}{T} \frac{\overline{U_p}}{\theta_p} \right)_p. \quad (7)$$

480 where  $\Omega$ ,  $\theta$  and  $R_d$  being the Earth's angular frequency, potential temperature and  
 481 dry gas constant, respectively. The subscripts  $\varphi$  and  $p$  represent the partial derivatives with  
 482 respect to latitude and pressure, respectively. The overbars indicate temporal and zonal  
 483 averages. From Eq. (6), the increase of zonal wind will narrow the range of Rossby  
 484 wave numbers that can propagate into the stratosphere (Charney and Drazin, 1961; Xu  
 485 et al., 2024).

486 As shown in Fig. 9, positive *RFI* values for both zonal wavenumbers 1 and 2 are  
 487 found over the northern mid- to high latitudes in EXP\_CTL, indicating that the basic-  
 488 state flow is favorable for the upward propagation of planetary waves (Figs. 9a, 9c).  
 489 In EXP\_NHE, however, the *RFI* is generally reduced over the same region, especially  
 490 in the upper troposphere and lower stratosphere. These negative *RFI* anomalies suggest  
 491 that the strengthened background westerlies in the polar stratosphere make the  
 492 environment less conducive to the vertical propagation of Rossby waves (Figs. 9b, 9d).  
 493 Similar behavior is found for both wavenumber-1 and wavenumber-2 components,  
 494 although the wavenumber-1 signal appears more spatially coherent. Therefore, the  
 495 reduction of *RFI* provides a dynamical explanation for the weakened upward EP-flux  
 496 branch seen in Fig. 8b.

497 Physically, the revised OGWD scheme weakens the parameterized drag in the  
 498 northern polar stratosphere, which strengthens the local westerlies. Stronger  
 499 background westerlies narrow the range of planetary-wave numbers that can propagate  
 500 vertically into the stratosphere. Consequently, the upward propagation of resolved  
 501 Rossby waves is suppressed, and less resolved wave forcing reaches the polar

502 stratosphere. This effect acts together with the weakened parameterized OGWD to  
 503 reduce the easterly wind bias in the polar stratosphere. At the same time, the associated  
 504 redistribution of resolved wave forcing favors a weakening of the polar-tropospheric  
 505 westerlies, thereby contributing to the improvement of the large-scale circulation over  
 506 the northern high latitudes.



507

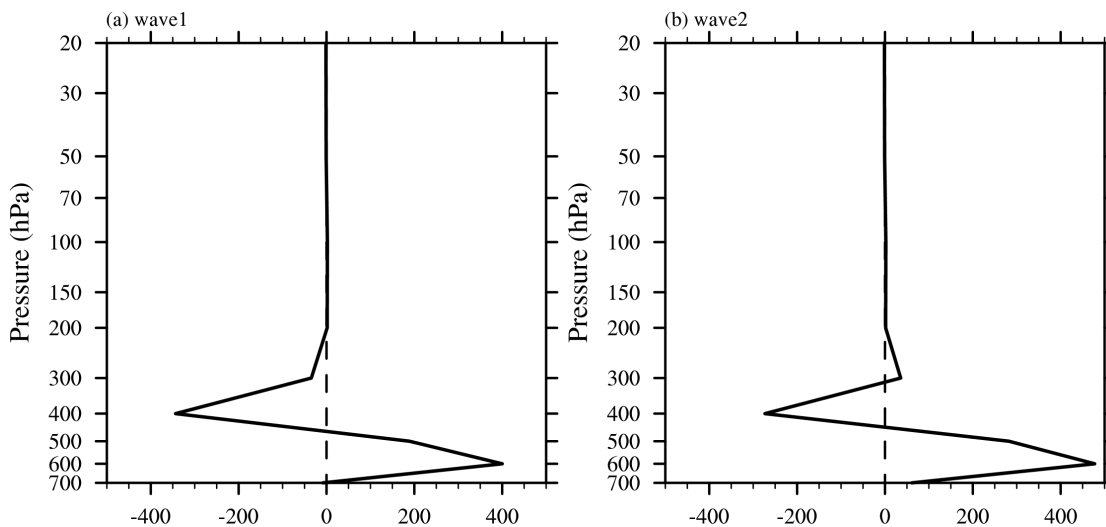
508 Figure 9. Refractive index for the (a) wavenumber-1 and (c) wavenumber-2 resolved  
 509 waves averaged over the period of 10 December 2023 to 10 January 2024 in the

510 EXP\_CTL experiment. (b) The difference between the refractive indices of  
 511 wavenumber 1 in EXP\_NHE and EXP\_CTL (EXP\_NHE minus EXP\_CTL). (d) As in  
 512 (b), but for wavenumber 2.

513

514 To provide a more robust diagnosis of the bulk propagation conditions, the zonal-  
 515 mean refractive-index diagnostic averaged over  $50^{\circ}$ - $80^{\circ}$ N is further presented in Fig.  
 516 10. The averaged *RFI* anomalies are positive mainly below about 500 hPa, whereas  
 517 negative anomalies dominate above 500 hPa for both wavenumber 1 and wavenumber  
 518 2. This vertical contrast is consistent with the EP-flux response in Fig. 8b. The lower-  
 519 tropospheric environment tends to favor the initial upward propagation of resolved  
 520 Rossby waves, while the upper-tropospheric and lower-stratospheric background state  
 521 becomes less favorable for their continued propagation into the stratosphere.

522



523

524 Figure 10. (a) The difference between the refractive indices of wavenumber 1 in  
 525 EXP\_NHE and EXP\_CTL (EXP\_NHE minus EXP\_CTL), averaged over  $50^{\circ}$ - $80^{\circ}$ N. (b)  
 526 as in (a), but for wavenumber 2.

527

#### 528 4. Summary and discussions

529

The latest China Meteorological Administration Global Forecast System (CMA-  
 530 GFS) v4.0 model has been upgraded to a higher resolution of  $0.125^{\circ}$  in 2023. However,

531 this high-resolution global model still uses the parameterization scheme of orographic  
532 gravity wave drag (OGWD) developed by Kim and Arakawa (1995; KA95) which is  
533 based on hydrostatic orographic gravity wave (OGW) theory. In this study, the KA95  
534 OGWD scheme is revised by taking into account the nonhydrostatic effect (NHE) on  
535 the surface wave momentum flux (WMF) of OGWs, according to the nonhydrostatic  
536 OGW theory derived in our earlier study of Xu et al. (2021). The performance of the  
537 revised OGWD scheme is then evaluated for the medium-range forecast of the CMA-  
538 GFSv4.0 model. Two sets of numerical experiments (i.e., EXP\_CTL and EXP\_NHE)  
539 are conducted by using the original KA95 scheme and the revised NHE scheme,  
540 respectively. In each numerical experiment, there are in total 31 forecasts of 10-day  
541 forecasts. In each numerical experiment, there are in total 31 independent 10-day  
542 forecasts which are initiated at 00 UTC on each day of December 2023.

543         The results show that the revised OGWD scheme can improve the medium-  
544 range forecast of large-scale circulation in the Northern Hemisphere (NH), especially  
545 in the high latitudes. The easterly biases of zonal-mean zonal wind in the NH  
546 stratosphere are reduced, with both the magnitude and location of the polar night jet  
547 being better captured. The underestimation of the East Asia subtropical jet (EASJ) is  
548 also alleviated. In contrast, the revised OGWD scheme shows little influence on the  
549 stratospheric circulation in the Southern Hemisphere (SH). This is because, in boreal  
550 winter (i.e., austral summer), there is hardly OGWD in the SH stratosphere owing to  
551 the effect of critical-level absorption, leading to comparatively smaller circulation  
552 responses. Therefore, the quantitative evaluation of forecast skill is mainly performed

553 for the NH, where the impact of the revised OGWD scheme is physically more  
554 pronounced and statistically more robust.

555 Quantitative evaluation is performed for the medium-range forecast skills in the  
556 NH, taking the ERA5 reanalysis dataset as reference. Both experiments showed lower  
557 geopotential height (GPH) at 500 hPa than ERA5 reanalysis, with the mean bias (MB)  
558 and root mean square error (RMSE) increasing with forecast lead time. EXP\_NHE  
559 initially has greater MB and RMSE than EXP\_CTL until the 6th forecast day, but these  
560 metrics decrease more rapidly afterwards, resulting in an 11.59% reduction in MB and  
561 a 5.06% reduction in RMSE by day 10. Over the total 10 forecast days, the MB and  
562 RMSE of the GPH 500 in the NH are reduced by 2.6% and 0.52%, respectively,  
563 indicating improved simulation of large-scale circulation in the NH. The improvement  
564 is more noticeable in the high latitudes north of about 60°N, where the MB and RMSE  
565 of GPH 500 are decreased by 31.18% and 15.93% at the 10th forecast day. Similar  
566 results are found for the sea level pressure (SLP) in the NH, the MB and RMSE of  
567 which are reduced by 34.29% and 8.33%, respectively, by day 10 in EXP\_NHE.

568 The dynamics responsible for the improvement of large-scale wind circulation are  
569 examined. The NHEs act to decrease the surface WMF of OGWs, which leads to a general  
570 weakening of the parameterized OGWD in the midlatitudes and high latitudes of the NH.  
571 This weakening of OGWD directly increases the zonal winds in the mid-latitude  
572 troposphere and polar stratosphere, reducing the easterly biases. The enhanced zonal wind  
573 in the polar stratosphere acts to narrow the range of large-scale Rossby wave numbers  
574 that can propagate into the stratosphere by reducing the refractive index of Rossby waves.  
575 The suppressed upward propagation of Rossby waves leads to greater convergence of

576 Eliassen-Palm (EP) flux (i.e., resolved wave forcing) in the NH polar troposphere, which  
577 decelerates the zonal winds and thus alleviates the westerly biases there.

578 To sum up, this study demonstrates that incorporating the NHE into the OGWD  
579 parameterization scheme can help improve the simulation of large-scale atmospheric  
580 circulation in high-resolution global NWP models, which is thus important for accurate  
581 weather forecasts and/or climate simulations. However, there are still some limitations in  
582 this work. For example, this study pays much attention to the medium-range forecast of  
583 large-scale circulation in winter of NH. To further validate its effectiveness and robustness,  
584 it is necessary to conduct more comprehensive evaluations of the nonhydrostatic OGWD  
585 scheme in various numerical models focusing on different weather and climate systems.  
586 Additionally, this work only takes into account the effects of NHE on the OGWD. Other  
587 factors such as the vertical wind shear could also greatly affect the OGWD (e.g., Xu et al.,  
588 2019; Xu et al., 2020; Zhang et al., 2025). While Xu et al. (2021) explored the  
589 nonhydrostatic OGWs generated in a constant flow, it remains unclear how the vertical  
590 wind shear affects the behavior of nonhydrostatic OGWs which needs further study.

591

592 *Code and data availability.* The China Meteorological Administration Global Forecast  
593 System (CMA-GFS) model is archived on Zenodo under  
594 <https://doi.org/10.5281/zenodo.18476721> (Zhang, 2026). The CMA-GFS outputs and the  
595 ERA5 reanalysis data used for the comparison, along with the codes for orographic gravity  
596 wave scheme are uploaded to <https://doi.org/10.5281/zenodo.18529537> (Zhang, 2026).

597

598 *Author contributions.* RRZ was responsible for formal analysis, writing the original draft

599 and visualization. ZZA carried out data analyses. XX developed the code and conducted  
600 the analysis. HLX and QYC provided the resources and data curation.

601

602 *Competing interests.* The contact author has declared that none of the authors has any  
603 competing interests.

604

605 *Acknowledgements.* The authors would like to express their sincere thanks to the  
606 anonymous referees.

607

608 *Financial support.* This work is mainly supported by the National Natural Science  
609 Foundation of China (grants no. U2342226, 42275163), the Joint Research Project for  
610 Meteorological Capacity Improvement (grant no. 22NLTSZ006), and Jiangsu  
611 Meteorological Observatory (grant no. KQ202502).

612

613

614 **References**

- 615 Alexander, M. J., Geller, M., McLandress, C., Polavarapu, S., Preusse, P., Sassi, F., Sato,  
616 K., Eckermann, S., Ern, M., Hertzog, A., Kawatani, Y., Pulido, M., Shaw, T.A.,  
617 Sigmond, M., Vincent, R. and Watanabe, S.: Recent developments in gravity-wave  
618 effects in climate models and the global distribution of gravity-wave momentum  
619 flux from observations and models, *Quarterly Journal of the Royal Meteorological*  
620 *Society*, 136, 1103-1124, <https://doi.org/10.1002/qj.637>, 2010.
- 621 Alpert, J.: Sub-grid scale mountain blocking at NCEP, 20th Conference on Weather  
622 Analysis and Forecasting/16th Conference on Numerical Weather Prediction,  
623 [https://ams.confex.com/ams/84Annual/techprogram/program\\_185.htm](https://ams.confex.com/ams/84Annual/techprogram/program_185.htm), 2004.
- 624 Beljaars, A. C. M., Brown, A. R., and Wood, N.: A new parametrization of turbulent  
625 orographic form drag, *Quarterly Journal of the Royal Meteorological Society*, 130,  
626 1327-1347, <https://doi.org/10.1256/qj.03.73>, 2004.
- 627 Booker, J. R., and Bretherton, F. P.: The critical layer for internal gravity waves in a shear  
628 flow, *Journal of Fluid Mechanics*, 27, 513-539,  
629 <https://doi.org/10.1017/S0022112067000515>, 1967.
- 630 Charney, J. G., and Drazin, P. G.: Propagation of planetary-scale disturbances from the  
631 lower into the upper atmosphere, *Journal of Geophysical Research (1896-1977)*, 66,  
632 83-109, <https://doi.org/10.1029/JZ066i001p00083>, 1961.
- 633 Chen, J., Ma, Z., Li, Z., Shen, X., Su, Y., Chen, Q., and Liu, Y.: Vertical diffusion and  
634 cloud scheme coupling to the Charney-Phillips vertical grid in GRAPES global  
635 forecast system, *Quarterly Journal of the Royal Meteorological Society*, 146, 2191-  
636 2204, <https://doi.org/10.1002/qj.3787>, 2020.

- 637 Chen Q., Shen, X., Sun, J., and Liu, K.: Momentum budget diagnosis and the  
638 parameterization of subgrid-scale orographic drag in global GRAPES, *Journal of*  
639 *Meteorological Research*, 30, 771-788, <https://doi.org/10.1007/s13351-016-6033->  
640 [y](https://doi.org/10.1007/s13351-016-6033-y), 2016.
- 641 Chen, P., and Robinson, W. A.: Propagation of Planetary Waves between the Troposphere  
642 and Stratosphere, *Journal of Atmospheric Sciences*, 49, 2533-2545,  
643 [https://doi.org/10.1175/1520-0469\(1992\)049<2533:POPWBT>2.0.CO;2](https://doi.org/10.1175/1520-0469(1992)049<2533:POPWBT>2.0.CO;2), 1992.
- 644 Choi, H. J., and Hong, S. Y.: An updated subgrid orographic parameterization for global  
645 atmospheric forecast models, *Journal of Geophysical Research: Atmospheres*, 120,  
646 12445-12457, <https://doi.org/10.1002/2015JD024230>, 2015.
- 647 Cohen, N. Y., Gerber, E. P., and Buhler, O.: Compensation between resolved and  
648 unresolved wave driving in the stratosphere: Implications for downward control,  
649 *Journal of the Atmospheric Sciences*, 70, 3780-3798, <https://doi.org/10.1175/JAS->  
650 [D-12-0346.1](https://doi.org/10.1175/JAS-D-12-0346.1), 2013.
- 651 Dai, Y., Zeng, X., Robert, E. D., Baker, L., Bonan, G. B., Bosilovich, M. G., Denning A.  
652 S., Dirmeyer, P. A., Houser, P. R., Niu, G., Oleson, K. W., Schlosser, C. A., Yang,  
653 Z.: The Common Land Model, *Bulletin of the American Meteorological Society*,  
654 84, 1013-1024, <https://doi.org/10.1175/BAMS-84-8-1013>, 2003.
- 655 Edmon, H. J., Hoskins, B. J. and McIntyre, M. E.: Eliassen-Palm Cross Sections for the  
656 Troposphere, *Journal of Atmospheric Sciences*, 37, 2600-2616,  
657 [https://doi.org/10.1175/1520-0469\(1980\)037<2600:EPCSFT>2.0.CO;2](https://doi.org/10.1175/1520-0469(1980)037<2600:EPCSFT>2.0.CO;2), 1980.

- 658 Fritts, D. C., and Alexander, M. J.: Gravity wave dynamics and effects in the middle  
659 atmosphere, *Reviews of Geophysics*, 41, <https://doi.org/10.1029/2001RG000106>,  
660 2003.
- 661 Han, J., and Pan, H. L.: Revision of Convection and Vertical Diffusion Schemes in the  
662 NCEP Global Forecast System, *Weather and Forecasting*, 26, 520-533,  
663 <https://doi.org/10.1175/WAF-D-10-05038.1>, 2011.
- 664 Haynes, P. H., McIntyre, M. E., Shepherd, T. G., Marks, C. J., and Shine, K. P.: On the  
665 “Downward Control” of Extratropical Diabatic Circulations by Eddy-Induced  
666 Mean Zonal Forces, *Journal of Atmospheric Sciences*, 48, 651-678,  
667 [https://doi.org/10.1175/1520-0469\(1991\)048<0651:OTCOED>2.0.CO;2](https://doi.org/10.1175/1520-0469(1991)048<0651:OTCOED>2.0.CO;2), 1991.
- 668 Hersbach, H., Bell, B., Berrisford, P., et al: The ERA5 global reanalysis, *Quarterly Journal*  
669 *of the Royal Meteorological Society*, 146, 1999-2049,  
670 <https://doi.org/10.1002/qj.3803>, 2020.
- 671 Hong, S. Y., and Pan, H. L.: Nonlocal Boundary Layer Vertical Diffusion in a Medium-  
672 Range Forecast Model, *Monthly Weather Review*, 124, 2322-2339,  
673 [https://doi.org/10.1175/1520-0493\(1996\)124<2322:NBLVDI>2.0.CO;2](https://doi.org/10.1175/1520-0493(1996)124<2322:NBLVDI>2.0.CO;2), 1996.
- 674 Hu, D., Guo, Y., and Guan, Z.: Recent Weakening in the Stratospheric Planetary Wave  
675 Intensity in Early Winter, *Geophysical Research Letters*, 46, 3953-3962,  
676 <https://doi.org/10.1029/2019GL082113>, 2019.
- 677 Kim, Y. J.: Balance of drag between the middle and lower atmospheres in a global  
678 atmospheric forecast model, *Journal of Geophysical Research: Atmospheres*, 112,  
679 <https://doi.org/10.1029/2007JD008647>, 2007.

- 680 Kim, Y. J., and Arakawa, A.: Improvement of Orographic Gravity Wave Parameterization  
681 Using a Mesoscale Gravity Wave Model, *Journal of Atmospheric Sciences*, 52,  
682 1875-1902, [https://doi.org/10.1175/1520-](https://doi.org/10.1175/1520-0469(1995)052<1875:IOOGWP>2.0.CO;2)  
683 0469(1995)052<1875:IOOGWP>2.0.CO;2, 1995.
- 684 Kim, Y. J., and Doyle, J. D.: Extension of an orographic-drag parametrization scheme to  
685 incorporate orographic anisotropy and flow blocking, *Quarterly Journal of the*  
686 *Royal Meteorological Society*, 131, 1893-1921, [https://doi.org/10.1256/qj.04.160,](https://doi.org/10.1256/qj.04.160.2005)  
687 2005.
- 688 Kim, Y. J., Eckermann, S., and Chun, H. Y.: An overview of the past, present and future  
689 of gravity-wave drag parametrization for numerical climate and weather prediction  
690 models - Survey article, *Atmosphere-ocean*, 41, 65-98,  
691 <https://doi.org/10.3137/ao.410105>, 2003.
- 692 Klemp, J. B., and Durran, D. R.: An Upper Boundary Condition Permitting Internal Gravity  
693 Wave Radiation in Numerical Mesoscale Models, *Monthly Weather Review*, 111,  
694 430-444, [https://doi.org/10.1175/1520-0493\(1983\)111<0430:AUBCPI>2.0.CO;2,](https://doi.org/10.1175/1520-0493(1983)111<0430:AUBCPI>2.0.CO;2)  
695 1983.
- 696 Kruse, C. G., Smith, R. B., and Eckermann, S. D.: The Midlatitude Lower-Stratospheric  
697 Mountain Wave “Valve Layer”, *Journal of the Atmospheric Sciences*, 73, 5081-  
698 5100, <https://doi.org/10.1175/JAS-D-16-0173.1>, 2016.
- 699 Li, M., Xu, X., Teixeira, M. A. C., Xue, M., Xue, H., Zhu, K., and Huang, H.: Improved  
700 Orographic Gravity Wave Drag Parameterization Accounting for the  
701 Nonhydrostatic Effect in the Weather Research and Forecasting Model: Tests for

- 702 Short-Range Forecast of Northeast China Cold Vortices, *Monthly Weather Review*,  
703 152, 2623-2637, <https://doi.org/10.1175/MWR-D-24-0097.1>, 2024.
- 704 Li, R., Xu, X., Xu, X., Shepherd, T. G., and Wang, Y.: Importance of orographic gravity  
705 waves over the Tibetan Plateau on the spring rainfall in East Asia, *Science China*  
706 *Earth Sciences*, 66, 2594-2602, <https://doi.org/10.1007/s11430-023-1204-6>, 2023.
- 707 Lindzen, R. S.: Turbulence and stress owing to gravity wave and tidal breakdown, *Journal*  
708 *of Geophysical Research: Oceans*, 86, 9707-9714,  
709 <https://doi.org/10.1029/JC086iC10p09707>, 1981.
- 710 Liu, K., Chen, Q., and Sun, J.: Modification of cumulus convection and planetary boundary  
711 layer schemes in the GRAPES global model, *Journal of Meteorological Research*,  
712 29, 806-822, <https://doi.org/10.1007/s13351-015-5043-5>, 2015.
- 713 Lott, F., and Miller, M. J.: A new subgrid-scale orographic drag parametrization: Its  
714 formulation and testing, *Quarterly Journal of the Royal Meteorological Society*,  
715 123, 101-127, <https://doi.org/10.1002/qj.49712353704>, 1997.
- 716 Lu, Y., Wu, T., Xu, X., Zhang, L., and Chu, M.: Improved Simulation of the Antarctic  
717 Stratospheric Final Warming by Modifying the Orographic Gravity Wave  
718 Parameterization in the Beijing Climate Center Atmospheric General Circulation  
719 Model, *Atmosphere*, 11, 576, <https://doi.org/10.3390/atmos11060576>, 2020.
- 720 Lu, Y., Xu, X., Wang, L., Liu, Y., Wu, T., Jie, W., and Sun, J.: Machine Learning  
721 Emulation of Subgrid-Scale Orographic Gravity Wave Drag in a General  
722 Circulation Model with Middle Atmosphere Extension, *J. Adv. Model. Earth Syst.*,  
723 16, e2023MS003611, <https://doi.org/10.1029/2023MS003611>, 2024.

- 724 Ma, Z., Liu, Q., Zhao, C., Shen, X., Wang, Y., Jiang, J. H., Zhe, L., and Yung, Y.:  
725 Application and Evaluation of an Explicit Prognostic Cloud-Cover Scheme in  
726 GRAPES Global Forecast System, *Journal of Advances in Modeling Earth Systems*,  
727 10, 652-667, <https://doi.org/10.1002/2017MS001234>, 2018.
- 728 McFarlane, N. A.: The Effect of Orographically Excited Gravity Wave Drag on the General  
729 Circulation of the Lower Stratosphere and Troposphere, *Journal of Atmospheric*  
730 *Sciences*, 44, 1775-1800, [https://doi.org/10.1175/1520-](https://doi.org/10.1175/1520-0469(1987)044<1775:TEOOEG>2.0.CO;2)  
731 [0469\(1987\)044<1775:TEOOEG>2.0.CO;2](https://doi.org/10.1175/1520-0469(1987)044<1775:TEOOEG>2.0.CO;2), 1987.
- 732 McLandress, C., Shepherd, T. G., Polavarapu, S., and Beagley, S. R.: Is Missing  
733 Orographic Gravity Wave Drag near 60°S the Cause of the Stratospheric Zonal  
734 Wind Biases in Chemistry-Climate Models? *Journal of the Atmospheric Sciences*,  
735 69, 802-818, <https://doi.org/10.1175/JAS-D-11-0159.1>, 2012.
- 736 Miller, M. J., and Palmer, T. N.: Orographic gravity wave drag: Its parameterization and  
737 influence in general circulation and numerical weather prediction models,  
738 Presented at the ECWMF Workshop on Observation, Theory and Modelling of  
739 Orographic Effects 1, 283-333, 1986.
- 740 Morcrette, J. J., Barker, H. W. J., Cole, N. S., Iacono, M. J., and Pincus, R.: Impact of a  
741 New Radiation Package, McRad, in the ECMWF Integrated Forecasting System,  
742 *Monthly Weather Review*, 136, 4773-4798,  
743 <https://doi.org/10.1175/2008MWR2363.1>, 2008.
- 744 Palmer, T. N., Shutts, G. J., and Swinbank, R.: Alleviation of a systematic westerly bias in  
745 general circulation and numerical weather prediction models through an orographic

- 746 gravity wave drag parametrization, *Quarterly Journal of the Royal Meteorological*  
747 *Society*, 112, 1001-1039, <https://doi.org/10.1002/qj.49711247406>, 1986.
- 748 Scinocca, J., and McFarlane, N.: The parametrization of drag induced by stratified flow  
749 over anisotropic orography, *Quarterly Journal of the Royal Meteorological Society*,  
750 126, 2353-2393, <https://doi.org/10.1002/qj.49712656802>, 2000.
- 751 Shen, X., Su, Y., Hu, J., et al.: Development and Operation Transformation of GRAPES  
752 Global Middle-range Forecast System, *Journal of Applied Meteorological Science*,  
753 28, 1-10, <https://doi.org/10.11898/1001-7313.20170101>, 2017.
- 754 Shen, X., Wang, J., Li, Z., Chen, D., and Gong, J.: Research and operational development  
755 of numerical weather prediction in China, *Journal of Meteorological Research*, 34,  
756 675-698, <https://doi.org/10.1007/s13351-020-9847-6>, 2020.
- 757 Shen, X. S., Su, Y., Zhang, H. L., et al.: New version of the CMA-GFS dynamical core  
758 based on the predictor-corrector time integration scheme, *Journal of Meteorological*  
759 *Research*, 37, 273-285, <https://doi.org/10.1007/s13351-023-3002-0>, 2023.
- 760 Shutts, G.: Gravity-wave drag parametrization over complex terrain: The effect of critical-  
761 level absorption in directional wind-shear, *Quarterly Journal of the Royal*  
762 *Meteorological Society*, 121, 1005-1021, <https://doi.org/10.1002/qj.49712152504>,  
763 1995.
- 764 Sigmond, M., and Shepherd, T. G.: Compensation between resolved wave driving and  
765 parameterized orographic gravity wave driving of the Brewer-Dobson circulation  
766 and its response to climate change, *Journal of Climate*, 27, 5601-5610,  
767 <https://doi.org/10.1175/JCLI-D-13-00644.1>, 2014.

- 768 Smith, R. B.: The Influence of Mountains on the Atmosphere, In B. Saltzman (Ed.),  
769 Advances in Geophysics (Vol. 21, pp. 87-230): Elsevier, 1979.
- 770 Teixeira, M. A. C.: The physics of orographic gravity wave drag, *Frontiers in Physics*, 2,  
771 <https://doi.org/10.3389/fphy.2014.00043>, 2014.
- 772 van Niekerk, A., Vosper, S. B., and Teixeira, M. A. C.: Accounting for the three-  
773 dimensional nature of mountain waves: Parametrising partial critical-level filtering,  
774 *Quarterly Journal of the Royal Meteorological Society*, 149, 515-536,  
775 <https://doi.org/10.1002/qj.4421>, 2023.
- 776 Wei, P., Xu, X., Xue, M., Li, J., Zhao, K., and Zhang, Q.: Complex Terrain Causes Global  
777 Model Prediction Biases of 21.7 Zhengzhou Extreme Precipitation, *Science*  
778 *Bulletin*, <https://doi.org/10.1016/j.scib.2025.09.015>, 2025.
- 779 Xu, X., Zhou, X., Yang, K., Lu, Y., Zhang, R., Yang, B., Tang, J., Wang, Y.: Reducing  
780 Winter Precipitation Biases Over the Western Tibetan Plateau in the Model for  
781 Prediction Across Scales (MPAS) With a Revised Parameterization of Orographic  
782 Gravity Wave Drag, *Journal of Geophysical Research: Atmospheres*, 128,  
783 e2023JD039123, <https://doi.org/10.1029/2023JD039123>, 2023.
- 784 Xu, X., Li, R., Teixeira, M. A. C., and Lu, Y.: On the Momentum Flux of Vertically  
785 Propagating Orographic Gravity Waves Excited in Nonhydrostatic Flow over  
786 Three-Dimensional Orography, *Journal of the Atmospheric Sciences*, 78, 1807-  
787 1822, <https://doi.org/10.1175/JAS-D-20-0370.1>, 2021.
- 788 Xu, X., Teixeira, M. A. C., Xue, M., Lu, Y., and Tang, J.: Impacts of wind profile shear  
789 and curvature on the parameterized orographic gravity wave stress in the Weather

- 790 Research and Forecasting model, Quarterly Journal of the Royal Meteorological  
791 Society, 146, 3086-3100, <https://doi.org/10.1002/qj.3828>, 2020.
- 792 Xu, X., Wang, Y., and Xue, M.: Momentum Flux and Flux Divergence of Gravity Waves  
793 in Directional Shear Flows over Three-Dimensional Mountains, Journal of the  
794 Atmospheric Sciences, 69, 3733-3744, <https://doi.org/10.1175/JAS-D-12-044.1>,  
795 2012.
- 796 Xu, X., Xue, M., Teixeira, M. A. C., Tang, J., and Wang, Y.: Parameterization of  
797 Directional Absorption of Orographic Gravity Waves and Its Impact on the  
798 Atmospheric General Circulation Simulated by the Weather Research and  
799 Forecasting Model, Journal of the Atmospheric Sciences, 76, 3435-3453,  
800 <https://doi.org/10.1175/JAS-D-18-0365.1>, 2019.
- 801 Xu, X., Zhang, R., Teixeira, M. A. C., van Niekerk, A., Xue, M., Lu, Y., Xue, H., Li, R.,  
802 Wang, Y.: A Parameterization Scheme Accounting for Nonhydrostatic Effects on  
803 the Momentum Flux of Vertically Propagating Orographic Gravity Waves:  
804 Formulas and Preliminary Tests in the Model for Prediction Across Scales (MPAS),  
805 Journal of the Atmospheric Sciences, 81, 805-817, <https://doi.org/10.1175/JAS-D-23-0020.1>, 2024.
- 807 Xue, H., Shen, X., and Su, Y.: Parameterization of Turbulent Orographic Form Drag and  
808 Implementation in GRAPES, Journal of Applied Meteorological Science, 22, 169-  
809 181, <http://qikan.camscma.cn/en/article/id/20110206>, 2011.
- 810 Zängl, G.: Orographic Gravity Waves Close to the Nonhydrostatic Limit of Vertical  
811 Propagation, Journal of the Atmospheric Sciences, 60, 2045-2063,  
812 [https://doi.org/10.1175/1520-0469\(2003\)060<2045:OGWCTT>2.0.CO;2](https://doi.org/10.1175/1520-0469(2003)060<2045:OGWCTT>2.0.CO;2), 2003.

- 813 Zhang, R.: CMA-GFS Model. Zenodo [code], <https://doi.org/10.5281/zenodo.18476721>,  
814 2026.
- 815 Zhang, R.: CMA-GFS outputs. Zenodo [data set],  
816 <https://doi.org/10.5281/zenodo.18529537>, 2026.
- 817 Zhang, R., Lu, Y., Xu, X., and Wang, Y.: Impacts of wind profile shear and curvature on  
818 the parameterized orographic gravity wave stress in a middle atmosphere resolving  
819 general circulation model, *Journal of Advances in Modeling Earth Systems*, 17,  
820 e2024MS004232, <https://doi.org/10.1029/2024MS004232>, 2025.
- 821 Zhang, R., Xu, X., and Wang, Y.: Impacts of Subgrid Orographic Drag on the Summer  
822 Monsoon Circulation and Precipitation in East Asia, *Journal of Geophysical*  
823 *Research: Atmospheres*, 125, e2019JD032337,  
824 <https://doi.org/10.1029/2019JD032337>, 2020.
- 825 Zhong, S., and Chen, Z.: Improved wind and precipitation forecasts over South China using  
826 a modified orographic drag parameterization scheme, *Journal of Meteorological*  
827 *Research*, 29, 132-143, <https://doi.org/10.1007/s13351-014-4934-1>, 2015.  
828